

See discussions, stats, and author profiles for this publication at: <https://www.researchgate.net/publication/359579753>

Pneumatic and tendon actuation coupled multi-mode actuators for soft robots with broad force and speed range

Preprint · March 2022

CITATIONS

0

READS

215

6 authors, including:



Jiaqi Zhu

Huazhong University of Science and Technology

14 PUBLICATIONS 13 CITATIONS

[SEE PROFILE](#)



Yi Xu

Huazhong University of Science and Technology

21 PUBLICATIONS 74 CITATIONS

[SEE PROFILE](#)



Han Ding

Jilin University

436 PUBLICATIONS 8,034 CITATIONS

[SEE PROFILE](#)



Zhigang Wu

Uppsala University

128 PUBLICATIONS 5,439 CITATIONS

[SEE PROFILE](#)

Some of the authors of this publication are also working on these related projects:



Tool path generation, motion error model and control of multi-axis CNC machining [View project](#)



robotic belt grinding system for turbine blade [View project](#)

Pneumatic and tendon actuation coupled multi-mode actuators for soft robots with broad force and speed range

ZHU JiaQi, PU MengHao, CHEN Han, XU Yi, DING Han & WU ZhiGang*

¹ State Key Laboratory of Digital Manufacturing Equipment and Technology, Huazhong University of Science and Technology, Wuhan 430074, China

Received xxx, accepted xxx; published online xxx

Broad output force and speed ranges are highly desired for actuators to endow soft robots with high performance, thereby increasing the range of tasks they can accomplish. However, limited by their low structural stiffness and single actuation method, most of the existed soft actuators are still difficult to achieve a broad force and speed range with a relatively compact body structure. Here, we propose a pneumatic and tendon actuation coupled soft actuator (PTCSA) with multiple actuation modes, mainly composing of a multi-joint thermoplastic polyurethanes (TPU)-made skeleton sealed in a film sleeve. The TPU skeleton with certain structural stiffness combined with soft joints allows PTCSA to output small force and respond rapidly under pneumatic actuation, as well as output high force and flexibly regulate response speed under tendon actuation, therefore achieving a broad force and speed range with a compact structure. The multiple modes constructed from the two actuation methods with different force and speed properties can cover diverse application scenarios. To demonstrate its performance, PTCSA was further used to construct a soft robotic arm (with a maximum lifting speed of 198°/s and can easily lift a load of 200 g), an inchworm-inspired wheel-footed soft robot (moves at a high speed of 2.13 cm/s when unload or pulls a load of 300 g forward), and a soft gripper (can grasp diverse objects, from 0.1 g potato chips to an 850 g roll of Sn-0.7Cu wire, from a high-speed moving tennis ball to an upright pen). This work indicates the potential of combining multiple complementary actuation methods to improve the force and speed range of soft actuators, and may provide inspiration for related research.

soft actuator, tendon actuation, pneumatic actuation, broad force and speed range, multiple modes

Citation: Zhu J Q, Pu M H, Chen H, et al. Pneumatic and tendon actuation coupled multi-mode actuators for soft robots with broad force and speed range. *Sci China Tech Sci*, 2022.

1 Introduction

Soft robots, mainly composed of soft materials, have attracted tremendous interest in recent years due to their inherent capability to safely and naturally interact with humans and unstructured environments [1,2]. Among them, soft actuators are the core components of soft robots, and directly determine their overall performance. To achieve a high-performance soft robot that can handle diverse tasks, soft actuators that combine a broad force and speed range

into a compact body are highly desired [3]. For example, a robotic soft gripper with a broad force range proven capable of grasping diverse objects from delicate and lightweight potato chips to rigid and heavy dumbbells [3], while a soft gripper with a broad speed range can not only quickly catch a thrown baseball [4], but also slowly pinch a banknote [5]. There are various actuation methods with different properties have been proposed for soft robots [2], such as fluid actuation [6-8], tendon actuation [9,10], shape memory materials-based actuation [11,12], and dielectric elastomer actuation [13,14], etc. However, due to their soft bodies and the limitations of a single actuation method, the existed soft

*Corresponding author (email: zgwu@hust.edu.cn)

actuators are still difficult to achieve a broad force and speed range with a relatively compact body structure.

For output force, soft actuators usually exhibit gentle force exertion, which is difficult for traditional rigid robots. However, the softness of their bodies also greatly limits the upper limit of their output force. To improve this issue, numerous efforts have been made, and the current solutions mainly include: setting reinforcement structures such as origami [15,16] or bellows-like structures [17], introducing reinforcement materials such as fabrics [18], bellow sheath [19], and even rigid rings [20], and using materials with higher hardness such as thermoplastic polyurethanes (TPU) to construct soft actuators [21,22]. All of these solutions focus on enhancing the internal antagonism of the soft actuators during actuation to improve their structural stiffness, thereby increasing their output force, while the combined use of these solutions is very common in practical applications. For instance, Li *et al.* [23] proposed a fluid-driven origami-inspired artificial muscle that can generate stresses of ~600 kPa, and peak power densities over 2 kW/kg, all of which are already comparable to natural muscles, while Liu *et al.* [24] designed a flexible hybrid pneumatic actuator, which introduced a set of rigid rings to reinforce the elastic bladder and was proven to have high response speed and large output force (~10 N). Among these high force soft actuators, fluid actuation and tendon actuation are the two most popular ones, mainly due to their mature technical base and capabilities to output higher forces. However, limited by a single actuation method, the enhancement of these soft actuators is often accompanied by the sacrifice of their capability to output tiny forces. Additionally, these solutions have no significant help for improving the response speed range of soft actuators.

For response speed, different actuation methods can endow the soft actuators with different response characteristics. Among them, soft actuators based on fluid actuation (mainly pneumatic actuation) have high potential to achieve high response speed through a compact body structure. The fluid control system can be connected externally through tubes, and some measures such as reducing the amount of fluid needed for actuation [25] or introducing mechanically unstable structures [26,27] can be taken to weaken the effect of the viscous forces in tubes and valves. For instance, Kim *et al.* [28] presented fluid-driven dual-morphing soft architectures that can be used to build a fast deployable (<0.4 s) catcher; and Baumgartner *et al.* [29] designed a soft balloon actuator that can achieve a large volume change of 1398% and a high-speed area change rate of $2600 \text{ cm}^2\text{s}^{-1}$ within 20 ms. Besides fluid actuation, several other actuation methods based on smart soft materials can also achieve high response speeds, such as dielectric elastomer actuation [30], or magnetic actuation [31]. However, due to the nonlinear characteristics, it is still difficult for all these actuation methods to achieve precise and continuous adjustment of their response speed. In

contrast, motor-based tendon actuation can conveniently achieve wide-range continuous adjustment of soft actuator speed. For instance, Li *et al.* [32] proposed a pre-charged pneumatic soft actuator, which is retracted by tendons. The bending average angular speed of the actuator has a definite mathematical relationship with tendon pulling speed, and can be precisely and continuously adjusted by controlling the pulling speed. However, as the motor cannot be externally deployed like the fluid control system, to keep the soft robot body relatively compact and lightweight, a small-sized motor is usually preferred to achieve tendon control. Under such a constraint, except for adopting a few expensive high-performance motors, most economical small-sized ones have to trade-off between force and speed [33]. Specifically, when the motor torque is constant, the diameter of the reel is proportional to the speed and inversely proportional to the force, which makes many tendon-actuated soft robots have to sacrifice speed to obtain sufficient force. A feasible solution is to dynamically adjust the motor transmission ratio [33-35], but the existing methods are either difficult to achieve actively adjustment of the transmission ratio that is directly related to the force-speed characteristics, or the increased adjustment mechanism will lead to a more complex and bulky actuator body structure.

Combining different actuation methods with different characteristics into a soft machine to improve its overall performance/functionality has proven to be effective in recent years [36-41], where the combination of pneumatic and tendon actuation is one of the most common ones [38-41]. For instance, Kang *et al.* [38] presented a continuum robot employing tendon embedded pneumatic muscles. The pneumatic muscles are used to achieve large scale movements while the tendons are used for fine adjustment of position. Meanwhile, Meng *et al.* [39] proposed a tendon-driven soft gripper, whose fingers can be bent under the actuation of preloaded air pressure, and can be pulled apart by the tendons and then quickly released to achieve high-speed grasping. In addition, some other researchers also tried to use tendon actuation to help pneumatic joints store energy for rapid extension [40], or to regulate joint stiffness through the antagonism of the two actuation methods [41]. However, up to now, studies focusing on integrating different actuation methods to improve the output force and speed range of soft actuators are still rare.

In this paper, we propose a pneumatic and tendon actuation coupled soft actuator (PTCSA) that combines a broad force and speed range in a relatively compact body structure. The PTCSA mainly consists of a multi-joint TPU-made skeleton sealed in a film sleeve, and its behavior can be controlled individually by air pressure and tendon. The TPU skeleton has a certain structural strength and soft joints, which allows PTCSA to output small force and respond rapidly under pneumatic actuation, as well as

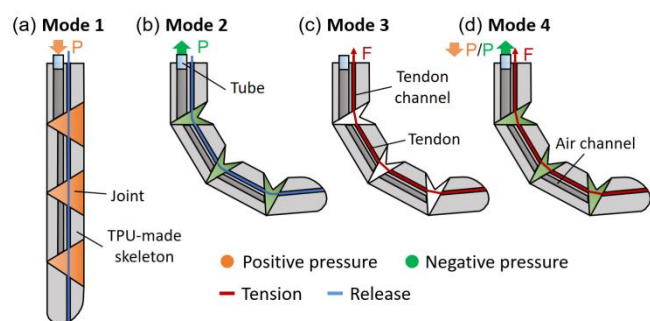


Figure 1 (Color online) Four typical actuation modes of PTCSA. (a) Actuated by positive pressure in Mode 1; (b) actuated by negative pressure in Mode 2; (c) actuated by tendon in Mode 3; (d) actuated by a combination of tendon and negative/positive air pressure in Mode 4. All schematics are cross-sectional views.

output high force and flexibly regulate response speed under tendon actuation with a compact body structure. The two actuation methods can be flexibly selected to form four actuation modes with varied force and speed properties, which can cover diverse application scenarios. We introduced the design and implementation of PTCSA, established its finite-element and theoretical models, and experimentally studied its deflection angle, response speed and output force. Finally, such PTCSAs were used to construct a soft robotic arm, an inchworm-inspired wheel-footed soft robot, and a soft gripper, all of which can achieve a broad force and speed range in a relatively compact body structure, thereby exhibiting multiple functions.

2 Design and Implementation

2.1 Design and working principle

As shown in Figure 1, the main body of PTCSA is a TPU skeleton with several wedge-shaped joints, sealed in a flexible but non-stretchable film sleeve. A tendon passes through the actuator along the tendon channel with its one end fixed to the tip of the skeleton. A tube fits with the air channel on the skeleton for air pressure control. By selectively controlling the tension of the tendon and the air pressure in the film sleeve, PTCSA can subsequently generate four different actuation modes for diverse scenarios:

- (1) When positive pressure is introduced into the film sleeve, the PTCSA will maintain or quickly return to its initial linear state. In this mode, the PTCSA exhibits high response speed and small output force, as shown in Figure 1(a).
- (2) When negative pressure is introduced into the film sleeve, the PTCSA will bend rapidly. In this mode, the PTCSA also exhibits high response speed and small output force, as shown in Figure 1(b).

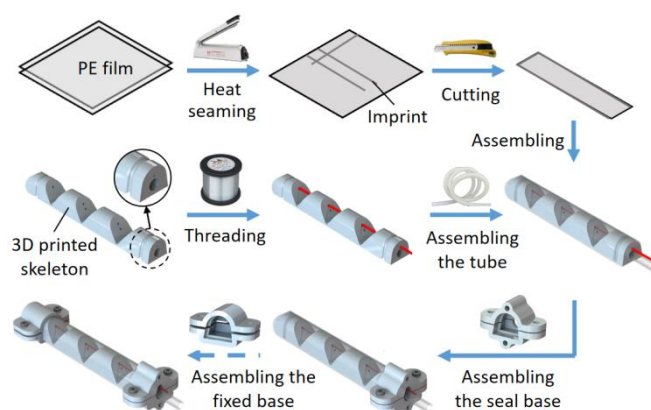


Figure 2 (Color online) Fabrication process. Solid arrows represent required steps, while dashed arrow represents optional step.

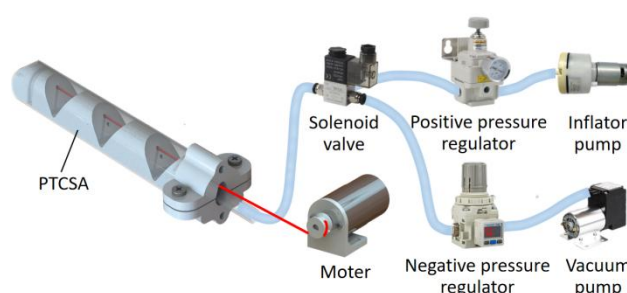


Figure 3 (Color online) Schematic diagram of control system.

- (3) When the tendon is tensed, the PTCSA will gradually bend. In this mode, the PTCSA exhibits high output force and continuously adjustable bending speed, as shown in Figure 1(c).
- (4) As shown in Figure 1(d), air pressure and tendon can also be controlled cooperatively temporally to deal with some scenarios with special requirements. For example, a soft gripper assembled with PTCSAs can first quickly catch a thrown ball under negative pressure, and then gradually tighten the tendons to further achieve a powerful grip. In addition, in some cases, to eliminate the effect of deflection hysteresis, positive pressure can also be introduced into the film sleeve during tendon tensioning.

2.2 Materials and fabrication of PTCSA

Figure 2 illustrates the fabrication process of the PTCSA. To allow the joints sufficiently bend under negative pressure and maintain a low bending stiffness, we choose flexible but non-stretchable polyethylene (PE) films (0.08 mm in thickness) as the material of the sealing sleeve. As shown in the figure, the PE film sleeve is fabricated by heat-sealing two stacked PE films according to the required size through a sealing machine, and then cutting off the useless part. Simultaneously, the skeleton is 3D printed with TPU, and a ring of sealing groove is set on its surface near the end. The

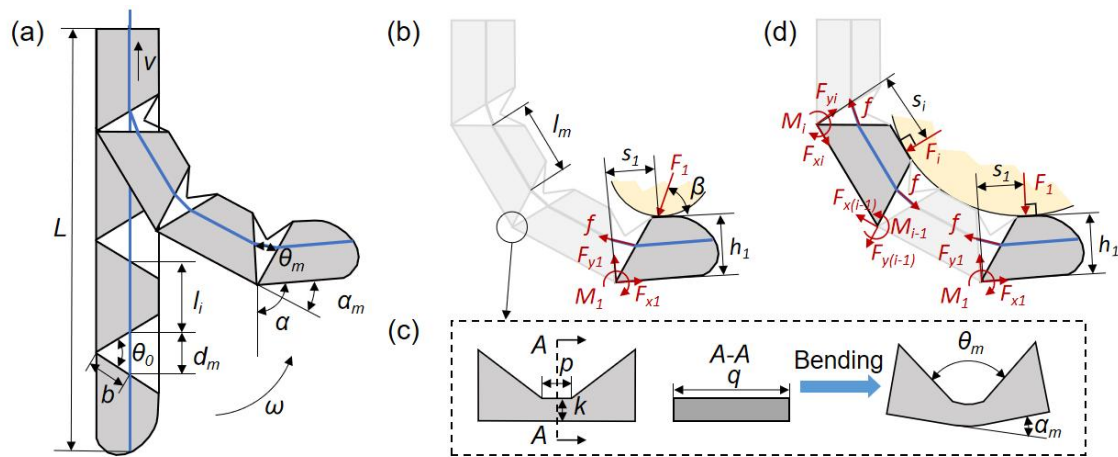


Figure 4 (Color online) Modelling and analysis. (a) Geometry dimensions of bent and unbent PTCSA; (b) force analysis and geometry dimensions when PTCSA is only subjected to an external force at its fingertip; (c) geometry dimensions of bent and unbent joint; (d) force analysis and geometry dimensions when PTCSA is subjected to multiple external forces perpendicular to its bone segments in the embracing pose.

TPU material endows the skeleton with a certain structural stiffness and soft joints, so that the PTCSA can output small force and respond rapidly under pneumatic actuation, as well as output high force and flexibly regulate response speed under tendon actuation. Before the skeleton is assembled with the film sleeve, fishing line (0.4 mm in diameter) and rubber tube (4 mm in outer diameter, 2 mm in inner diameter) are sequentially assembled with the skeleton through its tendon and air channels. Next, a set of rigid seal bases (their structure can be customized according to the actual needs) made of polylactic acid can be fastened to the end of the skeleton through bolts for air seal. If necessary, a ring of fixing grooves can be arranged at the tip of the skeleton and a set of rigid fixed bases can be assembled to realize the connection between the tip of the skeleton and other parts.

It should be noted that in order to improve the sealing effect of the tendon channel, the diameter of the tendon channel is designed to be similar to the diameter of the tendon, so that the air leakage can be effectively controlled. In future work, some more effective methods, such as oil seals or sealing rings, can be introduced to further enhance the sealing effect of tendon channel.

2.3 Control system of PTCSA

The control system of PTCSA is shown in Figure 3. It consists of a tendon control part and an air pressure control part. The tendon control part mainly includes a small-sized motor with a reel mounted on its shaft. The motor model can be flexibly selected according to the actual needs by comprehensively balancing torque, speed, size and cost, and a high reduction ratio motor with relatively low speed is usually selected to ensure sufficient output force of PTCSA.

Since the tendon needs to be tensioned during actuation, the motor is generally set close to the PTCSA. If necessary, several pulleys can be introduced to help change the direction of the tendon. The air pressure control part includes an inflating pump and a vacuum pump, which are used to provide positive pressure and negative pressure respectively. Two matching pressure regulating valves are installed on the two air paths to regulate the positive and negative pressures. A solenoid valve is used to switch the connection between PTCSA and the two air paths. If the PTCSA needs to switch between positive/negative pressure and atmospheric pressure, one of the pressure regulators can be set to 0.

3 Modeling

3.1 Finite-element model of PTCSA in Mode 2

Due to the nonlinear characteristics of soft materials, it is difficult to precisely describe the behavior of PTCSA under pneumatic actuation through analytical modeling, hence we developed a finite-element model in ABAQUS/CAE to quantitatively predict the deflection angle of PTCSA in Mode 2. The simulation process is introduced in this sub-section, and the simulation results will be compared with the experimental ones below.

First, we simplified the tendon channel on the PTCSA that might cause uneven meshes, and imported a simplified 3D model from SolidWorks into ABAQUS/CAE. The material parameters of the skeleton and sealing sleeve were then set. Specifically, the finger skeleton was modeled as a hyperelastic material, and the Yeoh constitutive model [42] ($C_{10}=28.5476$, $C_{20}=-0.0454$, $C_{30}=0$) was employed to simulate its behavior, while the sealing sleeve is made of PE

Table 1 Some key design parameters of PTCSA

Parameters	Value
Length of the tendon channel hole to the joint b	8 mm
Initial angle of the joint θ_0	75°
Length of the joint beam p	1.25 mm
Section width of the joint beam q	11.8 mm
Height of the joint beam k	0.8 mm
Length of the tendon channel in the middle bone segments l_m	13.3 mm

material with the Young's modulus of 90 MPa and Poisson's ratio of 0.4. Next, we meshed the two parts, wherein the skeleton mesh type is C3D4H, and the sealing sleeve mesh type is C3D4. We set a fixed constraint on the bottom end of the PTCSA, and gradually applied a negative pressure from 0 kPa to -80 kPa to the inner layer of the sealing sleeve. During this process, at each incremental 1 kPa increase in pressure, the deflection angle of PTCSA was measured.

3.2 Kinematic model of PTCSA in Mode 3

To better describe and control the performance of PTCSA in Mode 3, theoretical models were established. Some involved key design parameters are shown in Table 1.

For simplicity, assuming that (1) the joints are considered as a hinge point, and (2) the elastic elongation of the tendon during pulling and the elastic deformation of the bone segments are ignored, as shown in Figure 4(a), the tendon length within the soft actuator L can be expressed as,

$$L = \sum_{i=1}^{a+1} l_i + \sum_{m=1}^a d_m, \quad (1)$$

where l_i represents the length of the tendon in the i -th bone segment, d_m represents the length of the tendon in the m -th joint, a is the total number of joints. According to the trigonometric function, the length of the tendon in the m -th joint d_m can be calculated by,

$$d_m = b\sqrt{2-2\cos\theta_m}, \quad (2)$$

where b is the length of the tendon channel hole to the joint, θ_m is the angle of the m -th joint. By substituting Eq. (2) into Eq. (1), we can obtain,

$$L = \sum_{i=1}^{a+1} l_i + \sum_{m=1}^a b\sqrt{2-2\cos\theta_m}. \quad (3)$$

Based on the above equation, the length change of the tendon within the soft actuator ΔL can be calculated by,

$$\Delta L = b \sum_{m=1}^a (\sqrt{2-2\cos\theta_0} - \sqrt{2-2\cos\theta_m}), \quad (4)$$

where θ_0 is the initial angle of the joints. Additionally, the total deflection angle α of the PTCSA tip can be calculated by,

$$\alpha = \sum_{m=1}^a \alpha_m = \sum_{m=1}^a (\theta_0 - \theta_m), \quad (5)$$

where α_m represents the deflection angle of the m -th joint.

When PTCSA is unloaded, since the geometric dimensions and material properties of the joints are the same, the angles of its joints should also be the same. It can be expressed as,

$$\theta_1 = \theta_2 = \theta_3 = \dots = \theta_a. \quad (6)$$

By substituting Eq. (6) into Eq. (4), we can obtain the relationship between the length change of the tendon within the soft actuator ΔL and the angle of the m -th joint θ_m .

$$\theta_m = \arccos\left[1 - \frac{1}{2}\left(\sqrt{2-2\cos\theta_0} - \frac{\Delta L}{ab}\right)^2\right]. \quad (7)$$

Then, by substituting Eqs. (6) and (7) into Eq. (5), we can obtain the relationship between the length change of the tendon within the soft actuator ΔL and total deflection angle α of the PTCSA tip,

$$\alpha = a\theta_0 - a \arccos\left[1 - \frac{1}{2}\left(\sqrt{2-2\cos\theta_0} - \frac{\Delta L}{ab}\right)^2\right]. \quad (8)$$

Taking the derivation of both sides of the above equation with respect to time t , we can obtain the relationship between the PTCSA tip deflection angular velocity ω and the tendon pulling velocity v ,

$$\omega = \frac{v}{b\sqrt{1 - \frac{1}{4}\left(\sqrt{2-2\cos\theta_0} - \frac{\Delta L}{ab}\right)^2}}. \quad (9)$$

Since the length of the tendon is controlled by the winding motor, the length change of the tendon within the soft actuator ΔL can also be expressed as,

$$\Delta L = \pi d n \Delta t, \quad (10)$$

where d represents the diameter of the reel, n is the speed of the motor, Δt is the winding time of the motor. By substituting Eq. (10) into Eq. (8), we can obtain,

$$\alpha = a\theta_0 - a \arccos\left[1 - \frac{1}{2}\left(\sqrt{2-2\cos\theta_0} - \frac{\pi d n \Delta t}{ab}\right)^2\right]. \quad (11)$$

By substituting Eq. (10) into Eq. (9), we can obtain

$$\omega = \frac{\pi d n}{b\sqrt{1 - \frac{1}{4}\left(\sqrt{2-2\cos\theta_0} - \frac{\pi d n \Delta t}{ab}\right)^2}}. \quad (12)$$

3.3 Static models of PTCSA in Mode 3

For simplicity, we make some additional assumptions: (1) the effect of the film sleeve is negligible; (2) the friction between the tendon and the tendon channels is negligible. Firstly, we study the relationship between the fingertip force

and the tendon pulling force f when the PTCSA is only subjected to an external force F_l at its fingertip.

As shown in Figure 4(b), we perform force analysis on the tip bone segment, and its moment balance equation can be listed as,

$$M_1 + F_{1s_1} \sin \beta = F_l h_1 \cos \beta + f \sin \frac{\alpha_1}{2} b \sin \frac{\theta_0}{2} + f \cos \frac{\alpha_1}{2} b \cos \frac{\theta_0}{2}, \quad (13)$$

where M_l is the joint bending moment exerted on the tip bone segment, s_l and h_l are the horizontal and vertical distances from the external force F_l to the joint respectively, β is the horizontal angle of the external force F_l , α_1 is the deflection angle of the joint next to the tip bone segment.

As shown in Figure 4(c), the joint can be regarded as a rectangular section beam, and the bending moment generated during its bending process can be approximately expressed as,

$$\frac{M_m}{EI} = \frac{1}{\rho} = \frac{\alpha_m}{p}, \quad (14)$$

where M_m is the bending moment generated by the m -th joint, E is the elastic modulus, ρ is the bending curvature, p is the length of the joint beam, and I is the moment of inertia, which can be expressed by,

$$I = \frac{qk^3}{12}, \quad (15)$$

where q is the section width of the joint beam, k is the height of the joint beam. According to Eqs. (13)-(15), the relationship between the external force F_l and the tendon pulling force f can be obtained by,

$$F_l = \frac{fb \cos(\frac{\alpha_1 - \theta_0}{2}) - \frac{Eqk^3 \alpha_1}{12p}}{s_1 \sin \beta - h_1 \cos \beta}. \quad (16)$$

Then, a static model of the relationship between the embracing forces and tendon pulling force f is established when PTCSA is subjected to multiple external forces perpendicular to its bone segments in the embracing pose.

As shown in Figure 4(c), we first perform force analysis on the tip bone segment, and its force and moment balance equations can be expressed as,

$$F_{x1} = f \cos \frac{\alpha_1}{2}, \quad (17)$$

$$F_{y1} + f \sin \frac{\alpha_1}{2} = F_l, \quad (18)$$

$$M_1 + F_{1s_1} = f \sin \frac{\alpha_1}{2} b \sin \frac{\theta_0}{2} + f \cos \frac{\alpha_1}{2} b \cos \frac{\theta_0}{2}, \quad (19)$$

where F_{x1} and F_{y1} are the force components exerted by the joint on the tip bone segment. According to Eqs. (14)-(15),

and (17)-(19), the external force F_l and the force components F_{y1} can be obtained by,

$$F_l = \frac{fb}{s_1} \cos(\frac{\alpha_1 - \theta_0}{2}) - \frac{Eqk^3 \alpha_1}{12s_1 p}, \quad (20)$$

$$F_{y1} = F_l - f \sin \frac{\alpha_1}{2}. \quad (21)$$

Then, we perform a force analysis on the i -th middle bone segment ($i \geq 2$) except the tip and proximal bone segments, and list its force and moment balance equations as,

$$F_{xi} + f \cos \frac{\alpha_{i-1}}{2} = F_{x(i-1)} \cos \alpha_{i-1} - F_{y(i-1)} \sin \alpha_{i-1} + f \cos \frac{\alpha_i}{2}, \quad (22)$$

$$F_{yi} + f \sin \frac{\alpha_{i-1}}{2} + f \sin \frac{\alpha_i}{2} = F_{x(i-1)} \sin \alpha_{i-1} + F_{y(i-1)} \sin \alpha_{i-1} + F_i, \quad (23)$$

$$M_i + F_{is_i} + fb \cos \frac{\alpha_{i-1}}{2} \cos \frac{\theta_0}{2} + (F_{x(i-1)} \sin \alpha_{i-1} + F_{y(i-1)} \cos \alpha_{i-1})(l_m + 2b \sin \frac{\theta_0}{2}) = M_{i-1} + fb \cos \frac{\alpha_i}{2} \cos \frac{\theta_0}{2} + fb \sin \frac{\alpha_i}{2} \sin \frac{\theta_0}{2} + f \sin \frac{\alpha_{i-1}}{2} (l_m + b \sin \frac{\theta_0}{2}), \quad (24)$$

where F_{xi} , F_{yi} , $F_{x(i-1)}$, and $F_{y(i-1)}$ are the force components exerted by the joints on the middle bone segment, M_i and M_{i-1} are the joint bending moments exerted by the joints on the middle bone segment, F_i is the external force exerted on the middle bone segment, α_i and α_{i-1} are the deflection angles of the two joints at the proximal and distal ends of the middle bone segment, s_i is the horizontal distance from the external force F_i to the proximal joint, l_m is the length of the tendon channel in the middle bone segment. According to Eqs. (14)-(15), and (22)-(24), the force components F_{xi} , F_{yi} , and external force F_i can be expressed by,

$$F_{xi} = F_{x(i-1)} \cos \alpha_{i-1} - F_{y(i-1)} \sin \alpha_{i-1} + f \cos \frac{\alpha_i}{2} - f \cos \frac{\alpha_{i-1}}{2}, \quad (25)$$

$$F_{yi} = F_{x(i-1)} \sin \alpha_{i-1} + F_{y(i-1)} \sin \alpha_{i-1} + F_i - f \sin \frac{\alpha_{i-1}}{2} - f \sin \frac{\alpha_i}{2}. \quad (26)$$

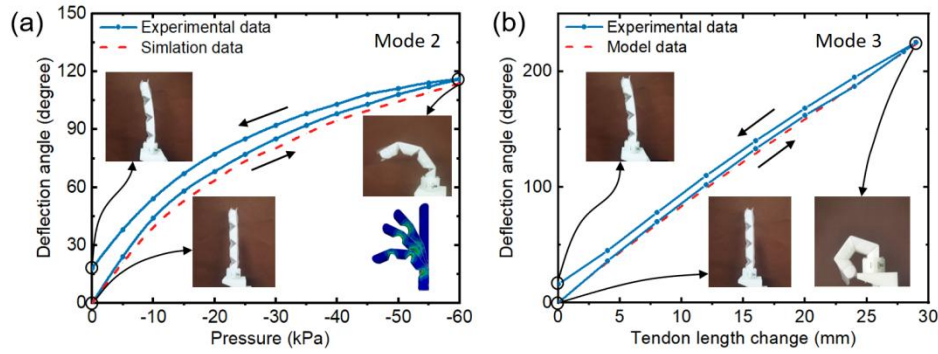


Figure 5 (Color online) Deflection angle test. (a) Deflection angle versus input air pressure of the PTCSA in Mode 2; (b) deflection angle versus tendon length change of the PTCSA in Mode 3.

$$F_i = \frac{1}{s_i} \left\{ +f \left[\begin{array}{l} \frac{Eqk^3(\alpha_{i-1} - \alpha_i)}{12p} \\ b \left(\cos \frac{\alpha_i - \theta_0}{2} - \cos \frac{\alpha_{i-1} + \theta_0}{2} \right) \\ + l_m \sin \frac{\alpha_{i-1}}{2} \end{array} \right] - \left(l_m + 2b \sin \frac{\theta_0}{2} \right) \begin{pmatrix} F_{x(i-1)} \sin \alpha_{i-1} \\ + F_{y(i-1)} \cos \alpha_{i-1} \end{pmatrix} \right\}, \quad (27)$$

Depending on the three recursive relational expressions of Eqs. (25)-(27), we can calculate the relationship between the external force F_i and the tendon pulling force f in turn from the second middle bone segment (the first bone segment is the tip bone segment), so as to finally get the embracing force (equal to the external force) on every bone segment of PTCSA.

In addition, when PTCSA is outputting fingertip or embracing force, it may sometimes occur that multiple bone segments stick together (ie, the joint angle is equal to 0°). At this time, the bone segments that are attached together can be regarded as a whole new bone segment to solve.

4 Experimental results

4.1 Deflection angle

We first studied the relationship between the tip deflection angle and the input air pressure or changes in tendon length of PTCSA. Tests were conducted by fixing the PTCSA and monitoring its tip deflection angle when the absolute value of applied air pressure or changes in tendon length gradually rise and fall. At the same time, the simulation results of PTCSA deflection angles under specified air pressure and the theoretical value of PTCSA deflection angles under specific changes in tendon length calculated according to Eq. (8) were plotted in Figure 5 for reference.

As shown in Figure 5(a), the deflection angle of PTCSA

increases with the increase of the absolute value of the input air pressure, and the simulation results agree well with the experimental ones. The deflection angle can reach 116° at an input air pressure of -60 kPa. Moreover, when the absolute value of air pressure gradually decreases, the deflection angle exhibits a certain hysteresis. The PTCSA can still maintain a deflection angle of 18° when the air pressure finally reaches 0 kPa. This is mainly because the TPU-made joints also underwent certain plastic deformation in addition to the elastic deformation during their bending process. To restore the deflection angle to 0° , a positive pressure can be applied to the PTCSA in Mode 1 to reset the joints to the initial angle.

In contrast, Figure 5(b) shows that the deflection angle of PTCSA has an approximately linear positive correlation with the changes in tendon length, and the experimental results agree well with the theoretical ones. The deflection angle can reach a theoretical maximum of 225° by gradually increasing the changes in tendon length. In addition, the PTCSA's deflection angle also shows a hysteresis in the decreasing process of the changes in tendon length, and it can still maintain at 16° when the changes in tendon length finally return to 0 . The reason of the hysteresis and the reset method of the deflection angle are the same as described above.

4.2 Response characteristics

A high-speed camera (Phantom V1212) was used to record its deflection angle changes as well to study its response speed. As shown in Figure 6(a), firstly, a fixed PTCSA was actuated to bend under different air pressures in Mode 2, and its deflection angle changes were recorded and plotted. The results indicate that the deflection angle of PTCSA can reach a stable value around 0.4 s at all six air pressures, and its growth rate shows a gradually decreasing trend. The slope of the deflection angle curve increases with the absolute value of the air pressure. It hints that a higher response speed can be obtained by increasing the absolute

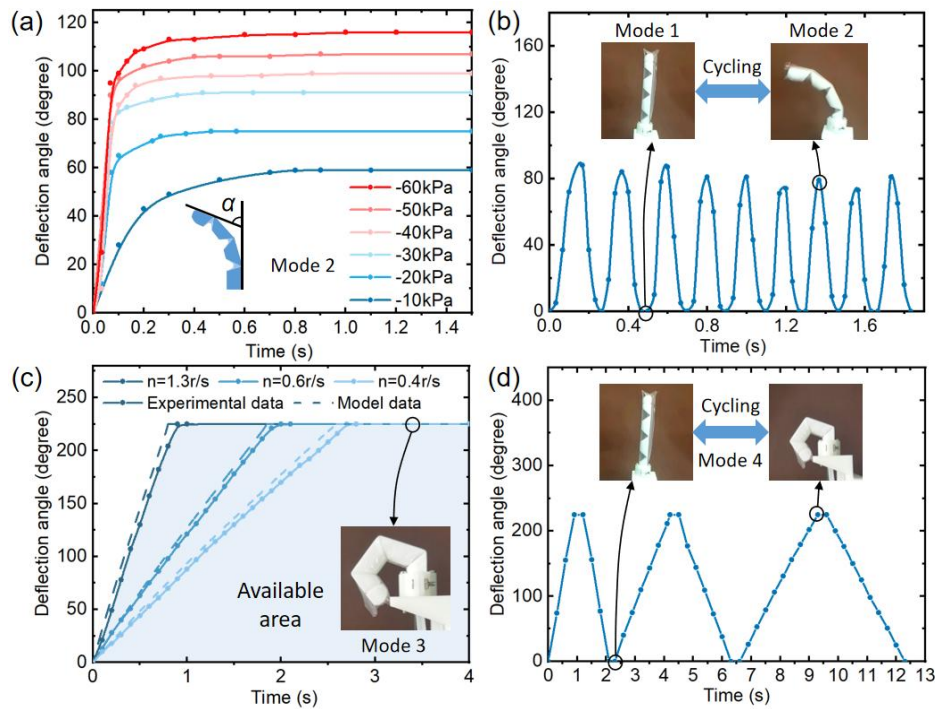


Figure 6 (Color online) Response characteristics test. (a) Deflection angle versus time of the PTCSA under different input air pressures in Mode 2; (b) deflection angle versus time during the high frequency switching of PTCSA between Modes 1 and 2; (c) deflection angle versus time of the PTCSA under different motor speeds in Mode 3; (d) deflection angle versus time during the response speed regulation process of PTCSA under tendon actuation in Mode 4.

Table 2 Parameters of several commercial small-sized motors

Motor specifications	Approximate sizes (mm)	Rated speed (r/s)	Rated torque (N/mm)	Minimum reel diameter (mm)	Maximum tendon force (N)
GM25BLDC2418, 1:9.3	24.4×24.4×37	5.58	15	9.8	1.53
GM1215BY, 1:10	152×2.5×24.2	5	4	10.9	0.37
GM16050S, 1:35	15.5×15.5×37.9	5.92	50	9.2	5.43
GM25BY, 1:4.4	25×25×33.8	6.63	25	8.25	3.03

value of the input air pressure. When the input air pressure is -60 kPa, the deflection angle of PTCSA can jump to 95° in the first 0.067 s, and its starting response speed can reach a considerable $1418^\circ/\text{s}$. Since the output force of motors is inversely proportional to their winding speed, to obtain such a high PTCSA response speed, small-size motors have to greatly sacrifice their output force. Specifically, according to Eq. (11), we can calculate that the condition for PTCSA to achieve the same response speed in Mode 3 is that the product of the reel diameter d and the motor speed n is 54.7. To meet such a demand, we randomly select four motors from the homepage search results of high-performance small-size motors in Taobao, completed the determination of their specifications and the diameters of the reels, and listed the calculated maximum tendon force they can produce in Table 2. As shown in the table, as a trade-off, the maximum tendon force that the motors can provide will be very limited. Therefore, we can use pneumatic to help

achieve high response speed and select high transmission ratio motors to ensure the sufficient output force of PTCSA.

To further demonstrate the high response speed of PTCSA in pneumatic modes, we let it switch between Modes 2 and 1 at a high frequency, and recorded the changes of deflection angle during this process. As shown in Figure 6(b), when the input air pressures are -40 kPa and 40 kPa, respectively, the PTCSA can oscillate at a frequency of 4 Hz, and its peak deflection angle can reach about 85° .

In contrast, by adjusting the motor speed, the response speed of PTCSA in Mode 3 can be flexibly and continuously adjusted over a broad range, although its upper limit is relatively low. Here, we chose a digital steering engine (DG-995) with an 8 mm diameter reel to experimentally study the response speed of PTCSA in Mode 3. As shown in Figure 6(c), we fixed the PTCSA and actuated it to bend at three different motor speeds, of which

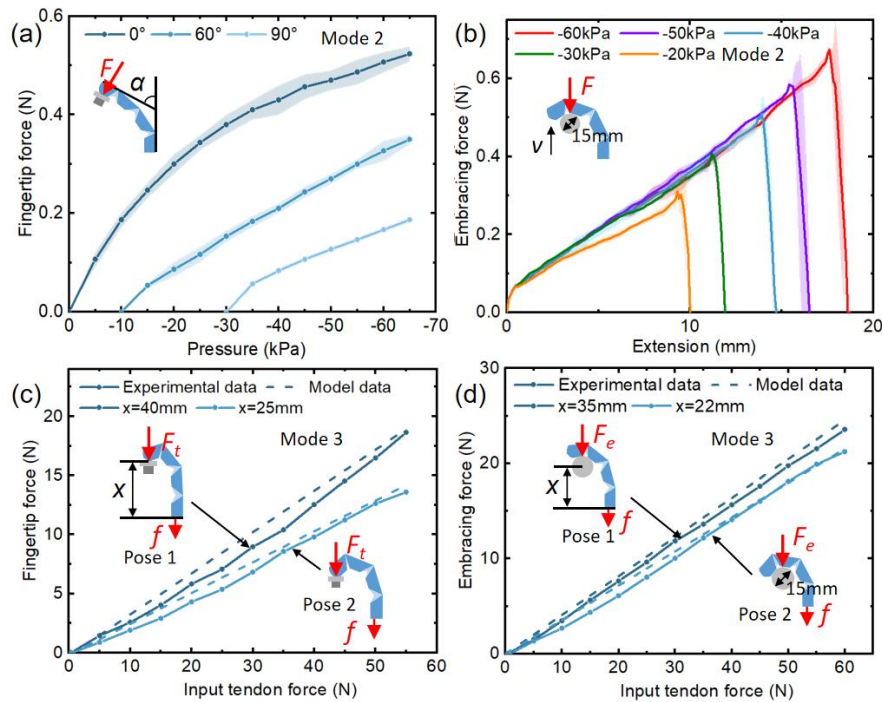


Figure 7 (Color online) Output force test. (a) Fingertip force versus input air pressure of the PTCSA at different deflection angles in Mode 2; (b) embracing force versus displacement of the PTCSA under different input air pressure in Mode 2; (c) fingertip force versus input tendon force of the PTCSA at different poses in Mode 3; (d) embracing force versus input tendon force of the PTCSA at different poses in Mode 3.

1.3 r/s is the fastest speed the steering engine could achieve, and the deflection angle changes were recorded and plotted. The theoretical deflection angle changes at specific motor speeds can be calculated according to Eq. (11) and was also plotted in the figure as reference. The results show that the deflection angle increases approximately linear, and can eventually reach the upper limit of 225° at different motor speeds. The theoretical data and the experimental data fit well at all motor speeds, which indicates the availability of the theoretical model. The slope of the deflection angle curve has a positive correlation with the motor speed. In fact, according to Eq. (11), the relationship between the two should be linear. At the upper limit motor speed of 1.3 r/s, the PTCSA can reach a response speed of about $260^\circ/\text{s}$. By continuously adjusting the motor speed, theoretically, the deflection angle curve of PTCSA in Mode 3 can cover the entire light blue area in Figure 6(c).

In addition, we also conducted experiments to further demonstrate the flexible adjustment of PTCSA's response speed under tendon actuation. As shown in Figure 6(d), the motor was controlled to rotate forward and reverse in turn at three different speeds, and the deflection angle changes were recorded and plotted. To eliminate the influence of the deflection angle hysteresis, a constant air pressure of 40 kPa was inputted into the PTCSA. The results show the good controllability of the response speed of PTCSA, which will facilitate the practical applications.

4.3 Output force

Experiments were conducted to test the output force of PTCSA in Mode 2. As shown in Figure 7(a), a force gauge (HANDPI, HP-10) was vertically pressed against the fingertip of PTCSA with its head, to test the relationship between the input air pressure and the fingertip force of PTCSA at three typical deflection angles (0° , 60° and 90°). During the tests at the latter two deflection angles, the PTCSA required a certain initial air pressure to bend to contact the preset force gauge head and begin to output force. The results show that the fingertip force of PTCSA has a positive correlation with the absolute value of the input air pressure and a negative correlation with the deflection angle. Under the air pressure of -65 kPa, the fingertip force of PTCSA with 0° deflection angle is about 0.52 N, and the fingertip force of PTCSA with 90° deflection angle is about 0.19 N. The low fingertip forces allow PTCSA to safely and gently interact with surrounding world with its fingertip. Moreover, as shown in Figure 7(b), the embracing force of PTCSA in Mode 2 was tested by an extension method. During the tests, a fixed PTCSA was actuated to wrap a 15mm diameter cylinder under different air pressure, and a force gauge (HANDPI, HP-10) rose at 1 mm/s to gradually pull the cylinder away from the PTCSA and record the output force changes. The results show that the embracing force of PTCSA is proportional to the absolute value of the input air pressure. The embracing

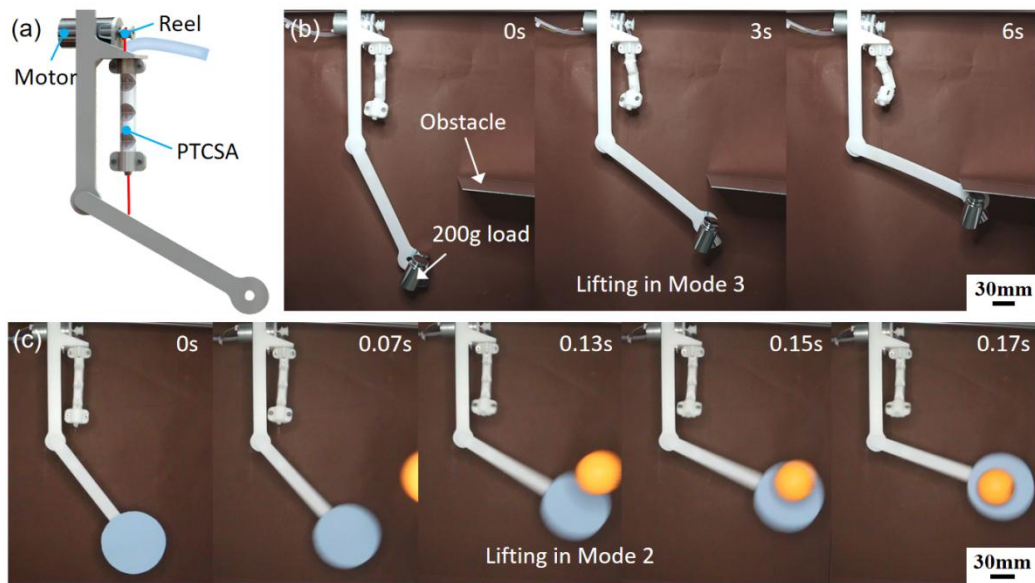


Figure 8 (Color online) An artificial-muscle-based robotic arm. (a) Structural design; (b) actual process of the robotic arm gradually lifting a 200 g load until it was blocked by the obstacle (Movie S1); (c) actual process of the robotic arm rapidly raising and intercepting a thrown ping pong ball (Movie S1).

force can reach a peak value of 0.67 N when the input air pressure is -60 kPa. Therefore, the PTCSA can also gently interact with the world in an embracing pose.

Then, tests were carried out to evaluate the output force of PTCSA in Mode 3. The theoretical curves of the output force versus tendon pulling force at specific poses can be calculated according to Eqs. (16), (20) and (27) and were also plotted in the figures as reference. As shown in Figure 7(c), firstly, we studied the relationship between the fingertip force and tendon pulling force of PTCSA under two typical fingertip press poses. During the tests, a force gauge (HANDPI, HP-100) was set horizontally, and a small initial tendon pulling force was required to bend the PTCSA to contact the force gauge head and begin to output force. The two poses can be distinguished by the different vertical distances from the force gauge head to the bottom of the PTCSA, which are 40 mm and 25 mm, respectively. The results show that the experimental results have approximately the same trend as the theoretical ones, and the deviations are mainly caused by the elastic deformation of the TPU skeleton when the PTCSA output force. The maximum deviation is up to about 1.5 N, which corresponds to 14% of the experimental value. The fingertip force is positively correlated with the tendon pulling force, and can finally reach 18.7 N in pose 1 when the tendon pulling force is 55 N. According to Eq. (16), theoretically, the relationship between the fingertip force and the tendon pulling force should be linear.

In addition, as shown in Figure 7(d), we also tested the embracing force of PTCSA in Mode 3 under two typical poses. During the tests, a fixed PTCSA was actuated to wrap a 15mm diameter cylinder suspended on a force gauge

(HANDPI, HP-100), and the two poses can be distinguished by different vertical distances from the center of the cylinder to the bottom of the PTCSA, which are 35 mm and 22 mm, respectively. The embracing force changes can be recorded by the force gauge as the tendon pulling force increases. The results indicate that the experimental results have approximately the same trend as the theoretical ones, and the slight deviations might be attributed to the same reason mentioned above. The maximum deviation is up to about 1 N, which corresponds to 16% of the experimental value. The embracing force is also positively correlated with the tendon pulling force and exhibits better linearity, which is consistent with the linear relationship between the two in the theoretical model. In pose 1, when the tendon pulling force is 60 N, the embracing force of PTCSA can finally reach 23.6 N, which is considerable compared to other soft actuators [22,43]. In practical applications, by selecting the motor reasonably, the PTCSA can output high force under tendon actuation and effectively interact with the external environment.

5 Demonstration of soft robots with broad force and speed range

5.1 Artificial-muscle-based soft robotic arm

Natural muscles can achieve a broad response speed and output force range with a compact soft structure. A muscle-driven human arm can not only move quickly to perform actions such as catching a ball, but also gradually and steadily lift heavy objects. Since our PTCSA has

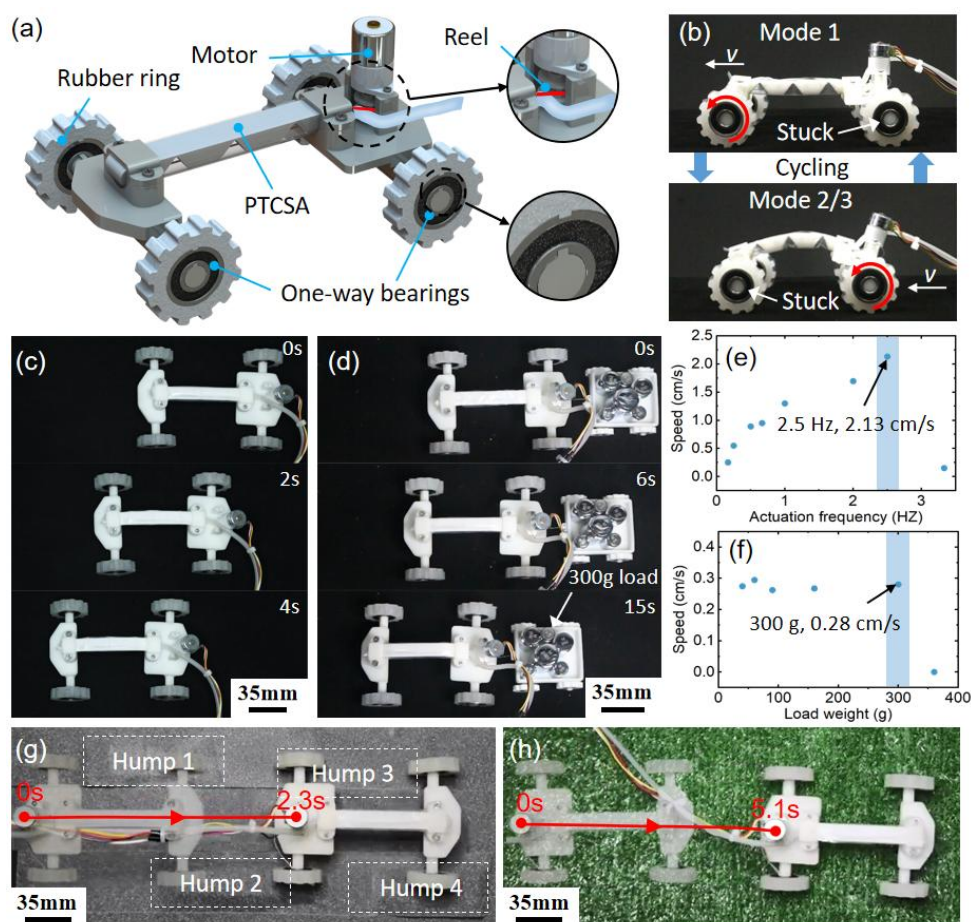


Figure 9 (Color online) An inchworm-inspired wheel-footed robot. (a) Structural design; (b) locomotion principle of the wheel-footed robot; (c) actual process of the rapid locomotion of the wheel-footed robot under no load (Movie S2); (d) actual process of the wheel-footed robot dragging a 300 g load (Movie S2); (e) locomotion speed versus actuation frequency of the wheel-footed robot switching between Modes 1 and 2; (f) locomotion speed versus load weight of the wheel-footed robot switching between Modes 1 and 3; (g) wheel-footed robot moves forward on an undulating terrain (Movie S2); (h) wheel-footed robot moves forward on an artificial turf (Movie S2).

muscle-like properties, we first used it to drive a robotic arm to rotate around an elbow joint, as shown in Figure 8.

As shown in Figure 8(a), a PTCSA was arranged vertically. Its proximal end was fixed to the upper arm through the seal bases, while its tip can move freely and was connected to the lower arm through a tendon tied to the fixed bases. The tendon extending from the PTCSA was wound around the reel of a motor (GM25BLDC2418, 1:125) fixed on the upper arm, while the tube extended distally and connected to the air pressure control system.

When the robot arm needs to lift heavy objects, the PTCSA can be actuated to bend in Mode 3, and its large output force and continuously adjustable speed allow it to steadily pull the loaded lower arm to rotate counterclockwise and move up. As shown in Figure 8(b), a load of 200 g can be steadily lifted during this process. In addition, due to the compliance provided by the PTCSA, the robotic arm can also have some buffer space when encountering unknown obstacles in the environment,

without directly causing problems such as rope breakage and motor damage. In contrast, when the robot arm needs to perform tasks such as high-speed interception, the PTCSA can be actuated to bend at high speed in Mode 2, and the lower arm can be pulled up by the PTCSA to achieve a rapid lift in a short time. Figure 8(c) demonstrates that the robotic arm was quickly lifted within 0.17 s under the actuation of PTCSA and successfully intercepted a thrown ping pong ball. During this process, the actuating air pressure of PTCSA was -60 kPa, and the maximum angular velocity of the lower arm can reach 198°/s.

5.2 Inchworm-inspired wheel-footed soft robot

The bow-crawling strategy of the inchworm is a classic locomotion mode in nature and has inspired the development of many soft robots for crawling [30]. A key feature of these robots is that they usually contain a bendable body with a pair of feet flanking it. When moving,

they anchor one of the feet and use the deformation of their body to push the other foot forward or backward. Such strategy is quite simple, and a wealth of principles are available to implement it. However, some problems such as poor terrain adaptability (steady anchoring of feet usually requires flat surface), low locomotion speed, and limited load-carrying capacity restrict the further application of these soft robots.

Here, based on PTCSA, we design an inchworm-inspired wheel-footed soft robot, as shown in Figure 9(a). The wheeled locomotion strategy can endow the robot with good terrain adaptability, while the PTCSA's wide force and speed range can enable the wheel-footed robot the capability of moving fast or dragging heavy objects forward. As shown in Figure 9(a), a PTCSA connects the front and rear segments of the wheel-footed robot. Each segment was fitted with a pair of wheels. The outer rubber rings of the wheels were matched with the axles through one-way bearings so that the wheels can only roll forward. A small motor (GM1215BY, 1:380) was set on the rear segment to control the PTCSA tendon. The tube of PTCSA was extended and connected to the distal air pressure control system.

When the wheel-footed robot needs to move forward, the PTCSA bends in Mode 2/3, and drags the rear segment forward under the frictional force of the stuck front wheels. Then, the PTCSA switches to Mode 1 to push the front segment forward under the friction force of the stuck rear wheels, thus completing a motion cycle, as shown in Figure 9(b). By making PTCSA switch between Modes 2 and 1 at high frequency, the wheel-footed robot can quickly move forward when unloaded, as shown in Figure 9(c). Moreover, the wheel-footed robot can also pull a heavy load forward with adjustable speed by making the PTCSA switch between Modes 3 and 1, as shown in Figure 9(d).

Experiments were carried out to study the performance of the wheel-footed robot on a black fabric road. As shown in Figure 9(e), the wheel-footed robot can achieve a peak locomotion speed of 2.13 cm/s at an actuation frequency of 2.5 Hz through the switching of PTCSA between Modes 1 and 2. During the tests, the input air pressures in the two modes were constant at 40 kPa and -60 kPa. By further increasing the absolute value of the air pressures, the locomotion speed of the robot is expected to be further improved. The decrease of locomotion speed at too high frequencies is mainly because the PTCSA cannot bend or straighten adequately in too short time intervals. Moreover, Figure 9(f) shows that the wheel-footed robot can pull a 300 g load forward at a speed of 0.28 cm/s through the switching of PTCSA between Modes 3 and 1. The input air pressure in Mode 1 was constant at 40 kPa, the actuation frequency was constant at 0.13 Hz, while the motor speed was constant at 8 rpm. According to the property of the load, the speed of the wheeled robot can be continuously adjusted by adjusting the motor speed. For example, when the load

becomes an item that needs to be carefully dragged, such as a glass of water, the wheeled robot can move forward at a slow speed, while in other cases, the motor speed can be increased to improve work efficiency. The load-carrying capacity of the wheeled robot is mainly limited by the friction of its front wheels, and its maximum load can be further increased by appropriately increasing its front segment weight.

In addition, we also selected two typical scenarios to test the terrain adaptability of this wheel-footed robot. The first scenario is an undulating terrain with a sandpaper surface, while the second scenario is an artificial turf with densely staggered grass blades on its surface. As shown in Figure 9(g) and (h), the experimental results demonstrate that the wheel-footed robot can well move forward in both scenarios. When traveling on undulating terrain, due to the softness of PTCSA, the wheel-footed robot can compliantly twist its body so that its four wheels can always be in contact with the surface.

5.3 Soft gripper

Robotic gripper is an essential part for robots to interact with their surrounding world. A desired robotic gripper can manipulate diverse objects and perform a wide variety of tasks with a relatively simple structure. Since PTCSAs can achieve a relatively broad force and speed range, we also use them to construct a three-finger soft robotic gripper with high versatility, as shown in Figure 10.

As shown in Figure 10(a), three PTCSAs were uniformly installed on the periphery of the gripper base through their seal bases. Their tendons were fixed on a reel controlled by a digital steering engine (DG-995, 25 kg), while their tubes extend out of the gripper along the hole reserved on the gripper base, and were connected to the distal air pressure control system.

When the gripper needs to manipulate some fragile and lightweight objects, the PTCSA can be actuated to bend in Mode 2, outputting gentle forces to avoid damaging the objects. As shown in the first row of Figure 10(b), such a gripper was proven to be able to safely grasp a fragile potato chip (1 g), a biscuit (9.3 g), a snack (23 g) and a plastic cup of water (96 g). Moreover, when the gripper needs to grasp some rigid and heavy objects, the PTCSA can be actuated to bend in Mode 3 to output high force to steadily lift objects. The second row of Figure 10(b) demonstrates that the gripper can also be used to grasp an apple (260 g), a bottle of hand sanitizer (500 g), and a roll of Sn-0.7Cu wire (850 g). According to our previous work [44], the maximum lifting force of this gripper in Mode 3 can reach 48.12 N, and its maximum force-to-weight ratio can reach 3512%, which are quite competitive among similar-sized soft grippers, as shown in Table 3. By replacing the current steering engine with a higher performance one, the maximum lifting force of the gripper

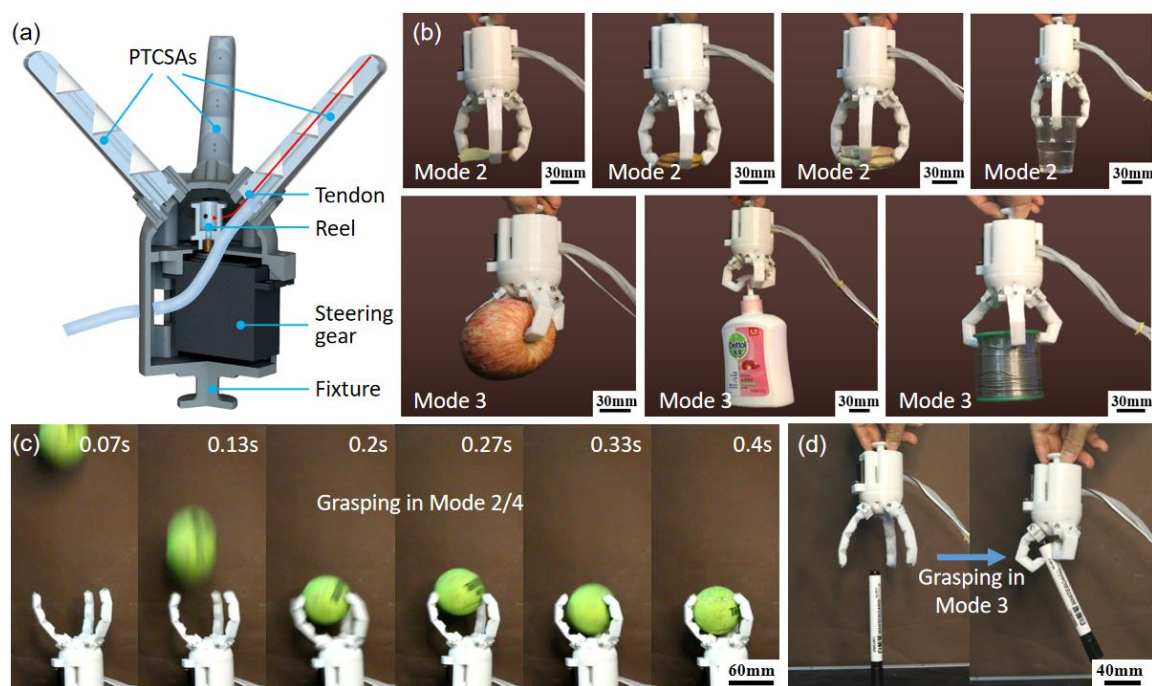


Figure 10 (Color online) A soft gripper. (a) Structural design; (b) grasping of a fragile potato chip (~1 g), a biscuit (9.3 g), a snack (23 g), a plastic cup of water (96 g), an apple (260 g), a bottle of hand sanitizer (500 g), and a roll of Sn-0.7Cu wire (850 g) (Movie S3); (c) the actual process of the gripper grasping a thrown tennis ball within 0.4 s (Movie S3); (d) the actual process of the gripper grasping an upright pen (Movie S3).

Table 3 Performance comparison of several soft grippers in recent years

Reference	Maximum lifting force (N)	Maximum force-to-weight ratio (%)	Year
This work	48.12	3512	2022
Tawk <i>et al.</i> [45]	31.31	706	2019
Subramaniam <i>et al.</i> [43]	30	-	2020
Xie <i>et al.</i> [7]	27	2400	2020
Cui <i>et al.</i> [46]	21	553	2021
Yan <i>et al.</i> [47]	14.6	760	2021

is expected to be further improved.

Besides the broad output force range, the broad speed range of PTCSAs can also expand the application range of this gripper. As shown in Figure 10(c), relying on the high response speed of PTCSAs in Mode 2, the gripper can successfully capture a rapidly falling tennis ball within 0.4 s. To obtain a firmer grip after the capture, the gripper can further switch to Mode 4 to produce a higher grasping force by tensing the tendons. Moreover, as shown in Figure 10(d), when the gripper needs to grab some special objects such as an upright pen, the unavoidable impact accompanied by high grasping speed can easily deflect or damage these objects, thus causing the failure of grasping. To avoid this, the gripper can carefully and relatively slowly complete the grip in Mode 3.

6 Discussion and conclusions

This article presents a pneumatic and tendon actuation coupled soft actuator called PTCSA, which can achieve a broad speed and force range with a compact body structure. Depending on the certain structural stiffness and soft joints of its TPU skeleton, the PTCSA can output gentle force and response rapidly under pneumatic actuation, as well as output high force and flexibly regulate response speed under tendon actuation. The two actuation methods can be flexibly selected and form four actuation modes with different force and speed characteristics, which are suitable for different application scenarios. The models of PTCSA are established, and experiments were conducted to study the various performance of PTCSA. The experimental results show that the PTCSA under pneumatic actuation can respond with a speed of up to 1418°/s, and can output gentle fingertip or embracing force below 1 N. In contrast, the PTCSA under tendon actuation was proven to have a continuously and precisely adjustable response speed and can output fingertip or embracing force of up to about 20 N. Based on the PTCSA, we built a soft robotic arm (with a maximum lifting speed of 198°/s and can easily lift a load of 200 g), an inchworm-inspired wheel-footed soft robot (moves at a high speed of 2.13 cm/s when unload or pulls a load of 300 g forward), and a soft gripper (can grasp diverse objects, from 0.1 g potato chips to a 850 g roll of Sn-0.7Cu wire, from a

high-speed moving tennis ball to an upright pen), all of which exhibit a broad force and speed range in a relatively compact body structure, and thus have diverse functions.

This work demonstrates the potential of combining multiple actuation methods with complementary properties to enhance the force and speed range of soft actuators simultaneously, and can provide a valuable reference for the development of high-performance soft robots in the future. Of course, it is surely that combining multiple actuation modes in a soft actuator will cause an increased overall system complexity, weight and volume, as well as a decrease in robustness. However, by designing reasonably or selecting proper actuation method (such as pneumatic actuation and magnetic actuation) whose control units can be externally set, we can still ensure a relatively compact body structure of the multi-modal soft actuator. Moreover, the high performance and multi-functionality of these multi-modal soft actuators can still make them a better choice in some demanding application scenarios, such as field exploration gripper and medical endoscope.

This work was supported by the National Natural Science Foundation of China (Grant No. 52188102 and U1613204).

- 1 Li S, Bai H, Shepherd R F, et al. Bio-inspired design and additive manufacturing of soft materials, machines, robots, and haptic interfaces. *Angew Chem Int Edit*, 2019, 58: 11182–11204
- 2 Zhu J, Lyu L, Xu Y, et al. Intelligent soft surgical robots for next-generation minimally invasive surgery. *Adv Intell Syst*, 2021, 3: 2100011
- 3 Zhu J, Chai Z, Yong H, et al. Bioinspired multimodal multipose hybrid fingers for wide-range force, compliant, and stable grasping. *Soft Robot*, 2022.
- 4 Lin Y, Zhang C, Tang W, et al. A bioinspired stress-response strategy for high-speed soft grippers. *Adv Sci*, 2021, 8: 2102539
- 5 Di Lallo A, Catalano M, Garabini M, et al. Dynamic morphological computation through damping design of soft material robots: application to under-actuated grippers. In: *Proceedings of the 2019 IEEE International Conference on Robotics and Automation (ICRA)*. Canada, 2019. 5155–5161
- 6 Jones T J, Jambon-Puillet E, Marthelot J, et al. Bubble casting soft robotics. *Nature*, 2021, 599: 229–233
- 7 Xie Z, Domel A G, An N, et al. Octopus arm-inspired tapered soft actuators with suckers for improved grasping. *Soft Robotics*, 2020, 7: 639–648
- 8 Jiao Z, Ji C, Zou J, et al. Vacuum-powered soft pneumatic twisting actuators to empower new capabilities for soft robots. *Adv Mater Technol*, 2019, 4: 1800429
- 9 Manti M, Hassan T, Passetti G, et al. A bioinspired soft robotic gripper for adaptable and effective grasping. *Soft Robotics*, 2015, 2: 107–116
- 10 Chen F, Xu W, Zhang H, et al. Topology optimized design, fabrication, and characterization of a soft cable-driven gripper. *IEEE Robot Autom Let*, 2018, 3: 2463–2470
- 11 Huang X, Kumar K, Jawed M K, et al. Soft electrically actuated quadruped (SEAQ)-Integrating a flex circuit board and elastomeric limbs for versatile mobility. *IEEE Robot Autom Let*, 2019, 4: 2415–2422
- 12 Wang W, Yu C Y, Abrego Serrano P A, et al. Shape memory alloy-based soft finger with changeable bending length using targeted variable stiffness. *Soft Robotics*, 2020, 7: 283–291
- 13 Li G, Chen X, Zhou F, et al. Self-powered soft robot in the Mariana Trench. *Nature*, 2021, 591: 66–71
- 14 Wang Y Z, Gupta U, Parulekar N, et al. A soft gripper of fast speed and low energy consumption. *Sci China Tech Sci*, 2019, 62: 31–38
- 15 Zhang Z, Fan W, Chen G, et al. A 3D printable origami vacuum pneumatic artificial muscle with fast and powerful motion. In: *Proceedings of the 2021 IEEE International Conference on Soft Robotics (RoboSoft)*. USA, 2021. 551–554
- 16 Liu S, Zhu Y, Zhang Z, et al. Otariidae-inspired soft-robotic supernumerary flippers by fabric kirigami and origami. *IEEE/ASME T Mech*, 2020, 26: 2747–2757
- 17 Tawk C, Spinks G M, in het Panhuis M, et al. 3D printable linear soft vacuum actuators: their modeling, performance quantification and application in soft robotic systems. *IEEE/ASME T Mech*, 2019, 24: 2118–2129
- 18 Zhu M, Do T N, Hawkes E, et al. Fluidic fabric muscle sheets for wearable and soft robotics. *Soft Robotics*, 2020, 7: 179–197
- 19 Fu H C, Ho J D L, Lee K H, et al. Interfacing soft and hard: a spring reinforced actuator. *Soft Robotics*, 2020, 7: 44–58
- 20 Gong S, Ding Q, Wu J, et al. Bioinspired multifunctional mechanoreception of soft-rigid hybrid actuator fingers. *Adv Intell Syst*, 2022: 2100242
- 21 Yap H K, Ng H Y, Yeow C H. High-force soft printable pneumatics for soft robotic applications. *Soft Robotics*, 2016, 3: 144–158
- 22 Keong B A W, Hua R Y C. A novel fold-based design approach toward printable soft robotics using flexible 3D printing materials. *Adv Mater Technol*, 2018, 3: 1700172
- 23 Li S, Vogt D M, Rus D, et al. Fluid-driven origami-inspired artificial muscles. *P Natl Acad Sci*, 2017, 114: 13132–13137
- 24 Liu X, Zhao Y, Geng D, et al. Soft humanoid hands with large grasping force enabled by flexible hybrid pneumatic actuators. *Soft Robotics*, 2021, 8: 175–185
- 25 Mosaddegh B, Polygerinos P, Keplinger C, et al. Pneumatic networks for soft robotics that actuate rapidly. *Adv Funct Mater*, 2014, 24: 2163–2170
- 26 Gorissen B, Melancon D, Vasios N, et al. Inflatable soft jumper inspired by shell snapping. *Sci Robot*, 2020, 5: eabb1967
- 27 Overvelde J T B, Kloek T, D'haen J J A, et al. Amplifying the response of soft actuators by harnessing snap-through instabilities. *P Natl Acad Sci*, 2015, 112: 10863–10868
- 28 Kim W, Byun J, Kim J K, et al. Bioinspired dual-morphing stretchable origami. *Sci Robot*, 2019, 4: eaay3493
- 29 Baumgartner R, Kogler A, Stadlbauer J M, et al. A lesson from plants: high-speed soft robotic actuators. *Adv Sci*, 2020, 7: 1903391
- 30 Gu G, Zou J, Zhao R, et al. Soft wall-climbing robots. *Sci Robot*, 2018, 3: eaat2874
- 31 Ren Z, Hu W, Dong X, et al. Multi-functional soft-bodied jellyfish-like swimming. *Nat Commun*, 2019, 10: 1–12
- 32 Li Y, Chen Y, Ren T, et al. Precharged pneumatic soft actuators and their applications to untethered soft robots. *Soft robotics*, 2018, 5: 567–575
- 33 O'Brien K W, Xu P A, Levine D J, et al. Elastomeric passive transmission for autonomous force-velocity adaptation applied to 3D-printed prosthetics. *Sci Robot*, 2018, 3: eaau5543
- 34 Matsushita K, Shikanai S, Yokoi H. Development of Drum CVT for a wire-driven robot hand. In: *Proceedings of the 2009 IEEE/RSJ International Conference on Intelligent Robots and Systems (IROS)*. USA, 2009. 2251–2256
- 35 Jeong S H, Kim K S. A 2-speed small transmission mechanism based on twisted string actuation and a dog clutch. *IEEE Robot Autom Let*, 2018, 3: 1338–1345
- 36 Zhang T, Yang L, Yang X, et al. Millimeter-scale soft continuum robots for large-angle and high-precision manipulation by hybrid

- actuation. *Adv Intell Syst*, 2021, 3: 2000189
- 37 Li C, Lau G C, Yuan H, et al. Fast and programmable locomotion of hydrogel-metal hybrids under light and magnetic fields. *Sci Robot*, 2020, 5: eabb9822
- 38 Kang R, Guo Y, Chen L, et al. Design of a pneumatic muscle based continuum robot with embedded tendons. *IEEE/ASME T Mech*, 2016, 22: 751–761
- 39 Meng J, Gerez L, Chapman J, et al. A tendon-driven, preloaded, pneumatically actuated, soft robotic gripper with a telescopic palm. In: *Proceedings of the 2020 IEEE International Conference on Soft Robotics (RoboSoft)*. USA, 2020. 476-481
- 40 Spröwitz A, Göttler C, Sinha A, et al. Scalable pneumatic and tendon driven robotic joint inspired by jumping spiders. In: *Proceedings of the 2017 IEEE International Conference on Robotics and Automation (ICRA)*. Singapore, 2017. 64-70
- 41 Shahid Z, Glatman A L, Ryu S C. Design of a soft composite finger with adjustable joint stiffness. *Soft Robot*, 2019, 6: 722-732
- 42 Han K, Kim N H, Shin D. A novel soft pneumatic artificial muscle with high-contraction ratio. *Soft Robot*, 2018, 5: 554-566
- 43 Subramaniam V, Jain S, Agarwal J, et al. Design and characterization of a hybrid soft gripper with active palm pose control. *Int J Robot Res*, 2020, 39: 1668-1685
- 44 Zhu J, Fei W, Ding H, et al. Pressure and tendon actuation integrated three-finger soft gripper for wide force and speed range grasping. In: *Proceedings of the 2021 International Conference on Mechatronics and Machine Vision in Practice (M2VIP)*. China, 2021. 682-687
- 45 Tawk C, Gillett A, in het Panhuis M, et al. A 3D-printed omni-purpose soft gripper. *IEEE T Robot*, 2019, 35: 1268-1275
- 46 Cui Y, Liu X J, Dong X, et al. Enhancing the universality of a pneumatic gripper via continuously adjustable initial grasp postures. *IEEE T Robot*, 2021, 37: 1604-1618
- 47 Yan J, Xu Z, Shi P, et al. A human-inspired soft finger with dual-mode morphing enabled by variable stiffness mechanism. *Soft Robot*, 2022, 9: 399-411